Astronomy & Astrophysics manuscript no. 3C273_draft
March 24, 2016
©ESO 2016

arXiv:1603.06989v1 [astro-ph.HE] 22 Mar 2016

Exploring the nature of broadband variability in the FSRQ 3C 273

C. Chidiac[1]⋆, B. Rani[1], T. P. Krichbaum[1], E. Angelakis[1], L. Fuhrmann[1], I. Nestoras[1], J. A. Zensus[1], A. Sievers[2], H. Ungerechts[2], R. Itoh[3], Y. Fukazawa[3], M. Uemura[4], M. Sasada[5], M. Gurwell[6], and E. Fedorova[7]

[1] Max-Planck-Institut für Radioastronomie (MPIfR), Auf dem Hügel 69, D-53121 Bonn, Germany
[2] Instituto de Radioastronomía Milimétrica (IRAM), Avenida Divina Pastora 7, Local 20, 18012 Granada, Spain
[3] Department of Physical Science, Hiroshima University, Higashi-Hiroshima, Hiroshima 739-8526, Japan
[4] Hiroshima Astrophysical Science Center, Hiroshima University, Higashi-Hiroshima, Hiroshima 739-8526, Japan
[5] Institute for Astrophysical Research, Boston University, 725 Commonwealth Avenue, Boston, MA 02215, USA
[6] Harvard-Smithsonian Center for Astrophysics, Cambridge, MA 02138, USA
[7] Astronomical Observatory of National Taras Shevchenko University of Kiev

Received ———; accepted ———-

ABSTRACT

Detailed investigation of broadband flux variability in the blazar 3C 273 allows us to probe the location and size of emission regions and their physical conditions. We report the results on correlation studies of the flaring activity in 3C 273 observed for a period between 2008 and 2012. The observed broadband variations were investigated using the structure function and the discrete correlation function methods. Starting from the common use of power spectral density analysis (PSD) at X-ray frequencies, we extended our investigation to characterize the nature of variability at radio, optical, and γ-ray frequencies. The PSD analysis showed that the optical/IR light curve slopes are consistent with the slope of white noise processes; while, the PSD slopes at radio, X-ray and γ-ray energies are consistent with red-noise processes. We found that the estimated fractional variability amplitudes have a strong dependence on the observed frequency. The flux variations at γ-ray and mm-radio bands are found to be significantly correlated. Using the estimated time lag of (110±27) days between γ-ray and radio light curves where γ-ray variations lead the radio bands, we constrained the location of the γ-ray emission region at a de-projected distance of 1.2 ± 0.9 pc from the jet apex. Flux variations at X-ray bands were found to have a significant correlation with variations at both radio and γ-rays energies. The correlation between X-rays and γ-rays light curves provides a hint of two possible time lags, which suggests presence of two components responsible for the X-ray emission. A negative time lag of -(50±20) days, where the X-rays are leading the emission, suggests X-rays are emitted closer to the jet apex from a compact region (0.02–0.05 pc in size) i.e. most likely from the corona at a distance of (0.5±0.4) pc from the jet apex. A positive time lag of (110±20) days (γ-rays are leading the emission) suggests jet-base origin of the other X-ray component at ∼ 4–5 pc from the jet apex. The flux variations at radio frequencies were found to be well correlated with each other such that the variations at higher frequencies are leading the lower frequencies, which could be expected in the standard shock-in-jet model.

Key words. galaxies: active – quasars: individual – quasars – radio continuum: galaxies – jets: galaxies – gamma-rays

1. Introduction

The Flat Spectrum Radio Quasar (FSRQ) 3C 273 is one of the most studied quasars since its discovery in 1963. It is a nearby source, with a red shift of 0.158 (Schmidt 1963). It is characterised by a jet close to the line-of-sight at a viewing angle of 5° − 11° (Liu & Shen 2009) and a maximum superluminal apparent velocity of v_{app} = 15 c (Lister et al. 2013). The jet, though extending up to kpc scales, remains collimated in all wavebands, from radio to X-rays, allowing the detailed study of the physical properties of the AGN starting from regions close to the supermassive black hole (SMBH) to the outer jet regions (Uchiyama et al. 2006).

The blazar 3C 273 is characterised by a strong radio emission from mm- to cm-wavelengths (Soldi et al. 2008). It has been suggested that this radio emission is caused by synchrotron emission of relativistic electrons in the jet, that could emit up to infrared (IR) frequencies (McHardy et al. 1999; Soldi et al. 2008). Türler et al. 1999 found that the sub-mm/radio flaring activity of the source is in agreement with the shock-in-jet model suggested by Marscher & Gear 1985. They also found that the high radio frequency outbursts are short-lived and are coming from a region closer to the jet apex than the long-lived low radio frequency outbursts.

Unlike other blazars that are highly polarised, 3C 273 has an average polarisation degree below 1% at optical frequencies (Valtaoja et al. 1991). The source is characterised by a blue bump due to the excess in the optical/UV emission. Two possible components have been suggested to explain the complex optical/UV spectrum. One rapidly variable component could be from the accretion disk (Shields 1978; Soldi et al. 2008), or illumination by an X-ray source (Ross & Fabian 1993) or a hot corona (Haardt et al. 1994). The second component seems to be related to synchrotron emission from the jet (Paltani et al. 1998). The IR emission in 3C 273 seems to be due to two variable components, (Paltani et al. 1998), where one component is due to thermal emission from the dusty torus and the other component is due to synchrotron emission from the jet (Robson et al. 1993; McHardy et al. 1999; Sokolov & Marscher 2005).

The source exhibits significant variations in the X-ray regime. Several studies have been carried out in order to understand the emission mechanisms and locate the radiation

⋆ Master student at Argelander Institut für Astronomie (AIfA) - University of Bonn

regions. Studies by McHardy et al. 1999; Grandi & Palumbo 2004; McHardy et al. 2007 suggested that a Seyfert-like component from the accretion disk is responsible for around 20% of the X-ray emission, while the rest could be due to a synchrotron self-Compton process, most likely, the up-scattering of the IR photons that had been produced by the synchrotron emission of the jet. Alternatively, the X-ray emission could be due to the comptonisation of the UV photons (Madsen et al. 2015).

The presence of a weak and neutral iron line in the X-ray spectrum suggests that the X-ray emission arises from the corona and reflection off the accretion disk (Madsen et al. 2015). The source therefore exhibits Seyfert-like properties in the X-ray regime (McHardy et al. 1999; Grandi & Palumbo 2004).

A previous study carried out on the multi-wavelength variability of 3C 273, found a correlation between the X-ray and the IR flares with the latter leading the former by a time lag of (0.75 ± 0.25) days (McHardy et al. 1999), which rules out the External Compton (EC) emission process as possible producer of X-Ray emission. This correlation was later confirmed by McHardy et al. 2007. Chernyakova et al. 2007 found a correlation between UV and X-rays; however, this correlation is still debatable since there are studies that failed to confirm it (Walter & Courvoisier 1992; Soldi et al. 2008). Many studies found for some sources a strong correlation between radio and γ-rays (Beaklini & Abraham 2014; Max-Moerbeck et al. 2014; Ramakrishnan et al. 2015), suggesting thus a common mechanism that is responsible for both radio and γ-rays. Moreover, the gamma-ray flares were accompanied by ejection of new components from the base of the jet (Jorstad et al. 2012).

The source was first detected in γ-ray frequencies by COS-B in 1970. Later, Energetic Gamma-ray Experiment Telescope (EGRET) on board Compton Gamma-Ray Observatory (CGRO) detected the source in 1991 at energies higher than 100 MeV (Hartman et al. 1992). *Fermi*/LAT (Large Area Telescope) detected 3C 273 since the beginning of its operation in 2008 (Abdo et al. 2010). In the period between July 2009 and April 2010, a strong flaring activity on GeV scales was reported. A ten-day flare was observed in August 2009 followed by two bright flares on 15-19 and 20-23 September 2009, which was followed by a sequence of rapid flares. The last flare was observed in April 2010 and since then the source went into a quiescent state that is lasting until the present day (Rani et al. 2013b). The fastest γ-ray flare had a doubling time-scale of 1.1 hour (Rani et al. 2013b). Following the episodes of extreme flaring activity in the source since 2008 (Rani et al. 2013b), we investigate the nature of the observed broadband flaring activity. In this paper, we carried out a detailed cross-correlation investigation across the electromagnetic spectrum to provide better constrains on the emission mechanisms. The key objective is to provide a better constrain on the location and size of emission region. This paper is structured as follows. In section 2, we explain the data used in this study. Section 3 presents the light curves, and we explain the methods applied in this paper, and the results of each method follow respectively. A discussion of the results is given in section 4. A conclusion is given in section 5.

2. Observations and data reduction

To explore the broadband flaring activity, we monitored the source using both space- and ground-based observing facilities for a time period between May 2008 and March 2012 (MJD= 54600 to 56000). In the following subsections, we summarise the observations and data reduction.

2.1. Gamma-ray data

The high energy GeV observations used in this study were obtained in a survey mode by *Fermi*-LAT. The data covered an energy range from 100 MeV to 300 GeV. Here we use the weekly and monthly averaged data of 3C 273 that are already presented in Rani et al. 2013b where the details of the observations and data reduction are discussed.

2.2. X-ray data

X-ray observations of the source were obtained by two space-based instruments: SWIFT and Rossi X-ray Timing Explorer (RXTE). The X-ray light curves cover three energy bands. The monthly averaged hard X-ray light curve, covering an energy range between 14 – 192 keV was observed by Swift-Burst Alert Telescope (BAT)[1] in both photon counting (PC) and windowed timing (WT) modes. Details of the observations and data reduction[2] are given in Stroh & Falcone 2013. Observations at 2 – 10 keV and 10 – 50 keV X-ray bands are provided by Rossi X-ray Timing Explorer - Proportional Counter Array (RXTE-PCA)[3]. The data are available for public use[4]. Details about the instrument and data reduction[5] are presented in Jahoda 1994.

2.3. Optical and IR data

Optical and IR light curves were provided by Small and Moderate Aperture Research Telescope System (SMARTS) monitoring programme[6]. SMARTS observes with telescopes located at Cerro Tololo Inter-american Observatory (CTIO). The monitoring programme aims to understand the high energy emission of blazars by searching for temporal correlation between flux and spectra of the major emission components. The observation and data reduction of the light curves can be found in Bonning et al. 2012. Observations by the 2.3 m Bok Telescope of Steward Observatory[7] complemented the optical data. The Steward observatory provides optical data in R and V bands for blazars and *Fermi* targets of opportunity sources. Details about the light curves produced in Steward Observatory can be found in Smith et al. 2009. The polarisation measurements are derived from the median Stokes Q and U values found from spectropolarimetry in a 5000-7000 Å bin. We also used optical photometric data from the Kanata Telescope in Hiroshima Observatory[8]. Details about the telescope and its instruments are referred to Uemura & Kanata Team 2009. Details of the observation and data reduction of the light curves can be found in Ikejiri et al. 2011.

2.4. Radio data

Radio band observations at 2.6, 5, 8, 10, 15, 23, 32, 43, 86, and 142 GHz were provided by the FERMI-GST AGN Multi-frequency Monitoring Alliance (F-GAMMA) pro-

[1] http://swift.gsfc.nasa.gov/results/bs70mon/SWIFT_J1229.1p0202
[2] http://www.swift.psu.edu/monitoring/readme.php
[3] http://heasarc.gsfc.nasa.gov/docs/xte/PCA.html
[4] http://www.swift.psu.edu/monitoring/source.php?source=3C273
http://cass.ucsd.edu/~rxteagn/3C273/3C273.html
[5] http://cass.ucsd.edu/~rxteagn/
[6] http://www.astro.yale.edu/smarts/glast/home.php
[7] http://james.as.arizona.edu/~psmith/*Fermi*/
[8] http://hasc.hiroshima-u.ac.jp/telescope/kanatatel-e.html

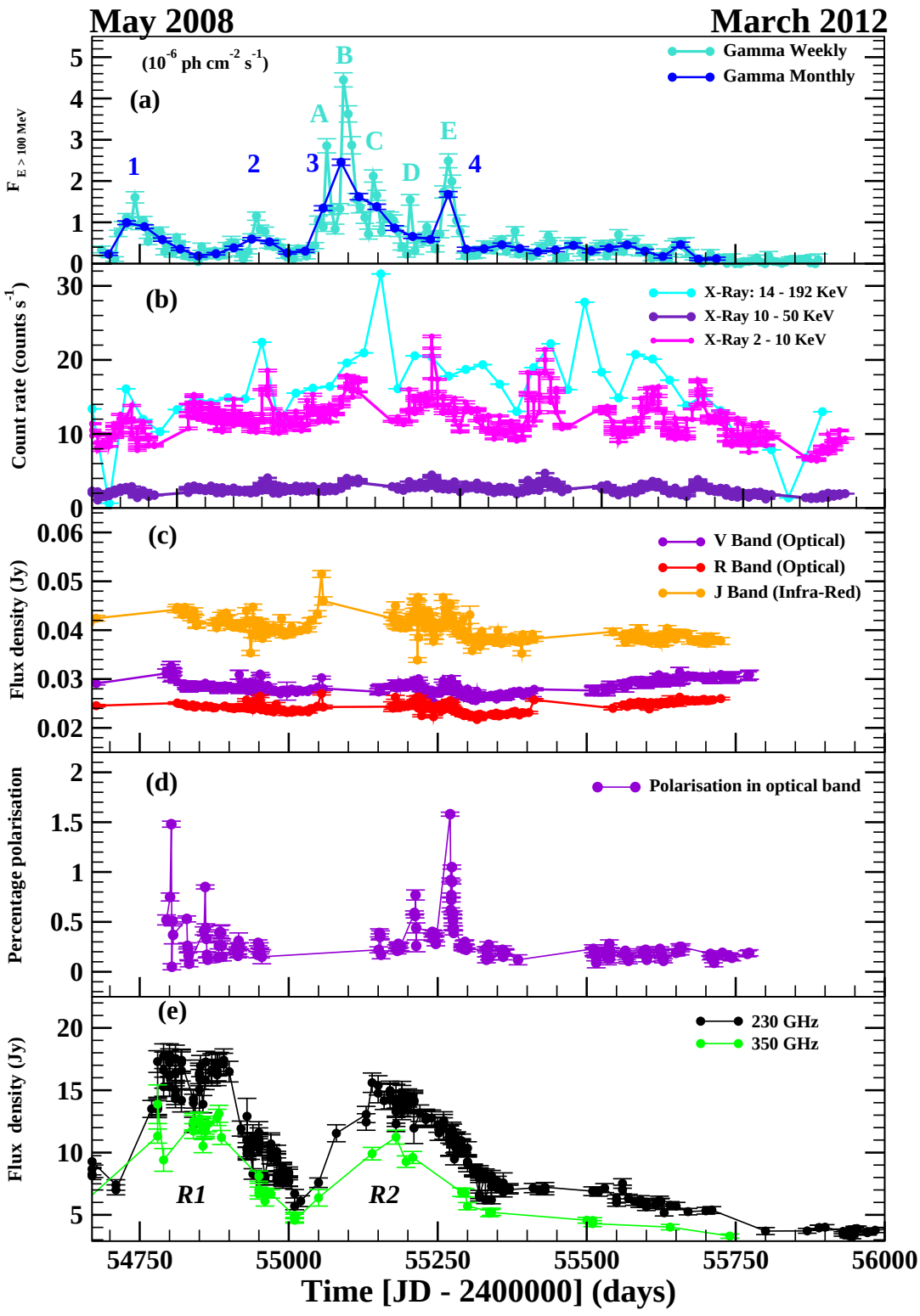

Fig. 1. Broadband light curves of 3C 273: (a) weekly (turquoise circles) and monthly (blue circles) averaged γ-ray light curves; (b) 14-192 keV band (cyan), the 10-50 keV band (indigo) and the 2-10 keV band (magenta) X-rays light curves; (c) optical (V and R passbands) and IR (J passband) light curves; (d) optical percentage polarisation curve; and (e) radio flux density curves at 230 GHz (in black) and 350 GHz (in green) bands.

gramme[9] (Fuhrmann et al. 2007; Angelakis et al. 2008). The F-GAMMA programme uses the Effelsberg 100 m telescope that covers a range from 2.6 to 43 GHz and the IRAM 30 m telescope at 86 and 142 GHz at Pico Veleta Observatory. The millimetre observations are closely coordinated with the more general flux density monitoring conducted by IRAM, and data from both programmes are included in this paper. The 230 and 350 GHz

[9] http://www3.mpifr-bonn.mpg.de/div/vlbi/fgamma/fgamma.html

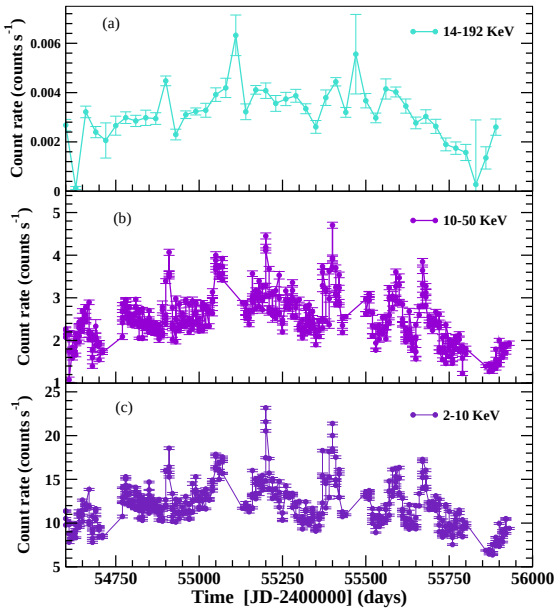

Fig. 2. X-ray light curves of 3C 273 at 14−192 keV (a), 10−50 keV (b), and 2−10 keV (c).

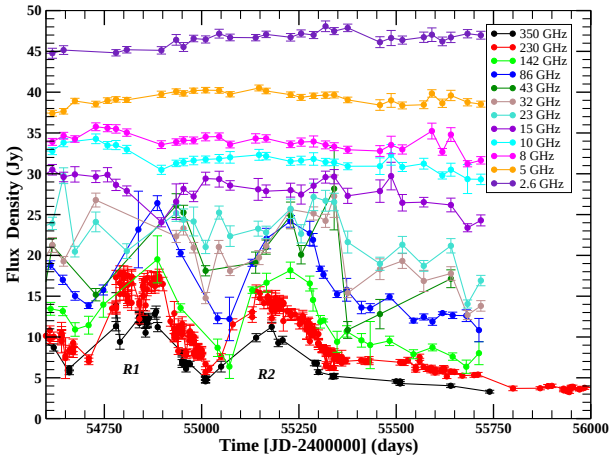

Fig. 3. Radio (cm to mm) bands light curves of 3C 273. Different colours represent different frequencies, from 2.6 GHz to 350 GHz (from top to bottom).

light curves are given by the SMA Observer Centre [10] data base (Gurwell et al. 2007).

3. Analysis and results

In this section, we present the statistical analysis of the observed broadband variations in 3C 273. We compare the fractional variability in each band as well as the variability time scale. To quantify the correlation between different frequencies, we employed the cross-correlation function method. Finally, we used the Power Spectral Density (PSD) method to get a better insight on the nature of the variability by describing the amount of variability as function of temporal frequency. The significance of the obtained results was tested via simulations. In the following subsections, we discuss the analysis in details.

3.1. Light curves analysis

Figures 1, 2 and 3 show the broadband light curves of 3C 273. Panel (a) in Fig. 1, shows the monthly averaged γ-ray light curve superimposed on top of the weekly averaged curve. The monthly sampled light curve shows fewer flares (labelled as 1 to 4) compared to the weekly sampled light curve. Apparently, the source seems to exhibit two different modes of flaring activity. A mode of slow activity (between MJD = 54600 to 55000) is followed by a second phase that is characterised by rapid and strong flaring activity (flare A to E) between 55050 and 55300 MJD. The source went to a quiescent state after flare E observed in April 2010, which is still persisting. The source also exhibited significant spectral variations during the flaring activity. At the beginning of each flare, the spectrum becomes harder, then softens again, at the end of the flare Rani et al. 2013b.

Similarly to the γ-ray regime, the source was active in X-ray bands (see Fig.1 b). Apparently, the flaring activity seems to be very similar in the three observed X-ray bands (Fig.2). As seen for the Swift-BAT light curve, there is a major flare that was observed almost simultaneously with flare (C) in the γ-ray flares. However, when the source went to a quiet state at γ-ray regime, it continued flaring at X-ray frequencies.

Figure 1 (c) shows the optical (R and V passbands) and IR (J passband) light curves. Unlike at γ-ray and X-ray energies, the optical/IR light curves of the source show lower amplitude fluctuations without pronounced peaks. The light curves have an almost constant flux during the entire period of observation. In addition to that the observed optical fractional polarisation is quite low (<2%). We however noticed significant variations in the polarisation curve (Fig. 1 d), indicative of an underlying non-thermal variable emission component. Apparently, the variations in optical polarisation became more pronounced during the γ-ray flaring activity. When the source went into a quiescent state in the GeV regime, no pronounced activity is noticed in the percentage polarisation curve.

Figure 1 (e) shows the light curves at 230 and 350 GHz, for the comparison of the variability of the mm-band with the variability in other energy bands. Figure 3 shows all the radio band light curves of the source. Higher radio frequencies from 23 GHz to 350 GHz show two flares: flare $\mathcal{R}_1$ between 54600 and 55050 MJD, and flare $\mathcal{R}_2$ between 55050 and 55600 MJD. At 230 and 350 GHz radio bands, we noticed sub-flaring activity on short time scales, superimposed on top of the major flare $\mathcal{R}_1$. This flare is observed simultaneously with the flares 1 and 2 in GeV regime while flare $\mathcal{R}_2$ is observed during the strong flaring period between 55000 and 55300 MJD at γ-rays frequencies. The flaring activity is less pronounced at frequencies below 23 GHz, which could be due to opacity. It is important to note that when the source was quiet in the GeV regime, the radio light curves did not show any prominent variations.

3.2. Fractional variability

We compute the fractional variability amplitude to compare the variations at different energy bands. Following Vaughan et al. 2003, we define the fractional variability as follows:

$$F_{var} = \sqrt{\frac{S^2 - \overline{\sigma_{err}^2}}{\bar{x}^2}} \quad (1)$$

where S^2 is the variance of the light curve, $\bar{x}$ is the mean value of the flux in the light curve, and $\overline{\sigma_{err}^2}$ its mean square error. The formal error of the fractional variability is estimated by

[10] http://sma1.sma.hawaii.edu/callist/callist.html

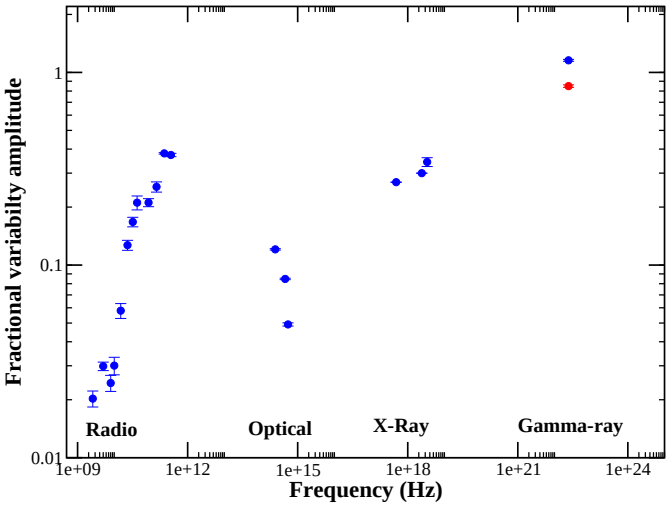

Fig. 4. Fractional variability amplitude plotted as a function of frequency. The red point describes the fractional variability amplitude of the monthly averaged γ-ray light curve.

(Vaughan et al. 2003, Appendix B):

$$err(F_{var}) = \sqrt{\frac{1}{2N}\left(\frac{\overline{err^2}}{F_{var}\times\overline{x}^2}\right)^2 + \frac{\overline{err^2}}{N}\times\frac{1}{\overline{x}^2}} \quad (2)$$

where $\overline{err^2}$ is the error on the flux. We adopted this method because it takes the uncertainty on the flux in account for calculating the variability amplitude as well as the error on it. By applying Eq. (1), we obtained an estimate of the fractional variability of all the light curves available for 3C 273. The estimated F_{var} amplitudes for the broadband light curves are plotted in Fig. 4.

As seen in Fig. 4, the variability amplitude for the radio light curves tends to increase with increasing frequency. This could be explained in terms of opacity effects i.e. at higher frequencies, we are probing the optically thin regions in the jet. There is less significant variability in the optical and IR light curves; as a consequence, the estimated fractional variability amplitudes at these bands are comparatively low. This could also be caused by the lack of data around the GeV flaring times. The fractional variability amplitude increases again in the X-ray regime, and is comparable to the fractional variability amplitude at mm-radio bands. The estimated F_{var} amplitudes are significantly higher for the γ-ray light curves exceeding 100%.

3.3. Structure function

We used the structure function (SF) method (Simonetti et al. 1985) to calculate the characteristic variability time scales in the light curves. For a given time series, the structure function (Simonetti et al. 1985) is defined as:

$$SF(\Delta t) = \frac{1}{N}\sum_{i=1}^{N}[x_i - x_{i+\Delta t}]^2 \quad (3)$$

where x_i is the flux at a given time, and $x_{i+\Delta t}$ is the flux at a time separation of Δt, and N is the number of data points that share a same Δt separation within a binning time interval. It is important to note that the SF breaks are not always reliable indicators of variability timescales Emmanoulopoulos et al. 2010. We therefore used the SF method only for comparison purposes; the estimated timescale are not used for any further calculations. Using eq. 3 we extracted the variability for all the light curves used in this study. The SF curves at 230 GHz and 2-10 keV bands are shown in Fig. 5; for the rest the SF curves are shown in Fig. A.3.

Table 1. Variability time scales as derived from the structure function analysis

Light curves	Variability time scale (days)
2.6 GHz	998±14
5 GHz	788±24
8 GHz	613±14
10 GHz	500±20
15 GHz	460±20
23 GHz	380±20
32 GHz	340±20
86 GHz	98±7
142 GHz	90±10
230 GHz	185±5
350 GHz	135±15
2-10 keV	225±15
10-50 keV	225±15
14-192 keV	228±14
Gamma-ray	90±10

As we can see for the 230 GHz SF curve (Fig. 5), the SF values increase as a function of time lag reaching a peak which is followed by a dip. The first SF peak corresponds to the shortest variability time scale and the dip indicates a possible time scale of periodic variation, if it is repeated (see Rani et al. 2009, for details). The estimated variability time scales at different energy bands are listed in Table 1. For the error on the time lag, we adopted half of the time binning as a conservative estimate.

As we can see in Fig. 6, the variability time scales at radio bands decrease as we go to higher frequencies. This implies that we are probing compact emission regions at short-mm bands, which are opaque to cm radio bands. In the optical bands, the fractional variability is very low. Therefore, the variability time scales cannot be determined with accuracy.

The variability time scales for the three X-ray light curves are very similar. For the light curves at 2-10 keV and 10-50 keV bands, we found a time scale of (226±15) days, and for the X-ray bands at 14-192 keV, we found a time scale of (228±15) days. These X-ray variability time scales are comparable to the variability time scales at mm-radio bands. In addition to that we noticed multiple cycles in the SF curves at both mm-radio and X-ray bands (see Fig. 5) which suggests nearly periodic variations at time scales of 350 – 400 days. Comparable time scales for variability and quasi-periodic oscillations at short-mm radio and X-ray regimes suggest a possible correlation between the two.

Using the SF analysis of the weekly averaged γ-ray light curve, we found a variability time scale of (91±10) days. However, it is important to note that the SF gives the time scale of the long term behaviour of the light curve. Interestingly, the estimated γ-ray variability time scale is comparable to that at 86 and 142 GHz radio bands (see Table 1), which could be a hint of a possible correlation between the radio and γ-ray bands. In Section 3.5, we investigate that in detail.

3.4. Power Spectrum Density (PSD)

To explore the nature of the variability, we used the Power Spectrum Density (PSD) analysis. The PSD method is explained in details in Vaughan et al. 2003 and Vaughan 2005. For an evenly

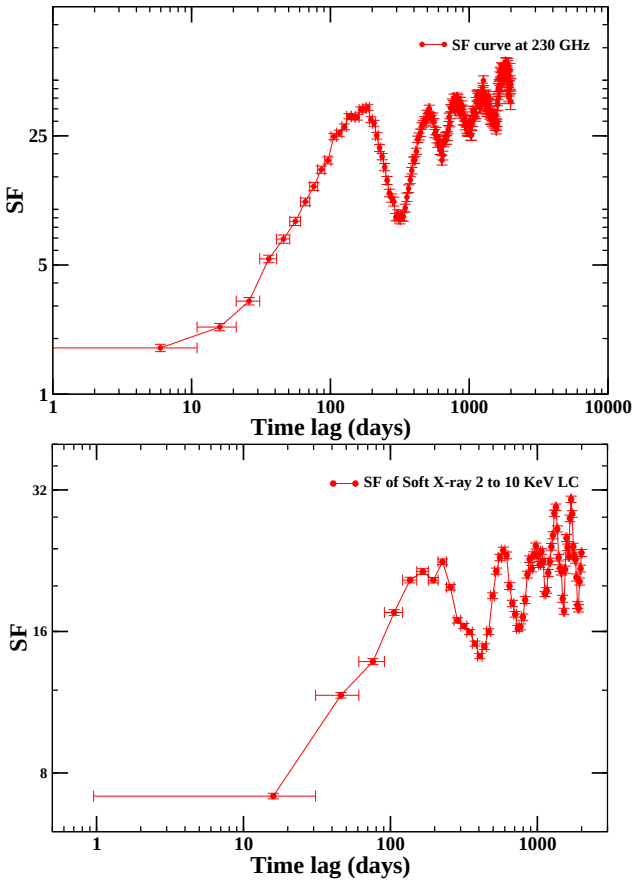

Fig. 5. Structure function at 230 GHz radio band (top) and 2-10 keV X-ray band (bottom).

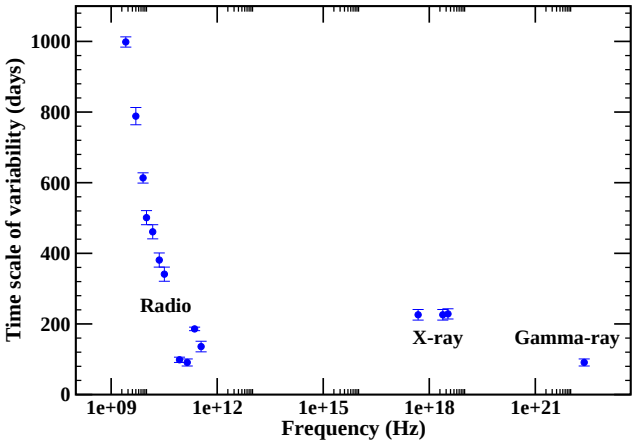

Fig. 6. Variability time scales plotted as a function of frequency (Hz).

sampled data set, the periodogram is the modulus-squared of the Discrete Fourier Transform (DFT) of the data. In a light curve with flux series x_i measured at discrete times t_i ($i = 1, 2, ..., N$), the modulus-square of the DFT is given as:

$$\left|DFT(f_j)\right|^2 = \left|\sum_{i=1}^{N} x_i e^{2\pi i f_i t_i}\right|^2 \quad (4)$$

at $\frac{N}{2}$ evenly spaced temporal frequencies $f_j = \frac{j}{N\Delta T}$ where $j = 1, 2, ...\frac{N}{2}$. The Nyquist frequency is: $f_{Nyq} = \frac{1}{2\Delta T}$. The periodogram $I(f_j)$ is given by:

$$I(f_j) = A\left|DFT(f_j)\right|^2 = \frac{2\Delta T}{N}\left|DFT(f_j)\right|^2 \quad (5)$$

The periodogram will be scattered around the true underlying power spectrum, if we are observing a noise process, following a χ^2 distribution with two degrees of freedom. The true power spectrum $P(f_j)$ is calculated as:

$$I(f_j) = P(f_j)\frac{\chi_2^2}{2} \quad (6)$$

3.4.1. Fitting the periodogram

The underlying power density spectrum can be described by a power law $P(f) = Nf^{-a}$ where a is the slope and N is the normalisation constant. We fitted the power law to the PSD using a least square fit method (LS) in log-scale. The scatter is multiplicative in linear-space, therefore it is additive in log-space, and identical at each frequency (Geweke & Porter-Hudak 1989; Papadakis & Lawrence 1993):

$$log\left[I(f_j)\right] = log\left[P(f_j)\right] + log\left[\frac{\chi_2^2}{2}\right] \quad (7)$$

Nonetheless, the expectation value of the periodogram in log-space is not the same as the expectation value of the spectrum. There is a bias between the two values. This bias is a constant due to the shape of the χ_2^2-distribution in log-space and it can be trivially removed.

$$\left\langle log\left[I(f_j)\right]\right\rangle = \left\langle log\left[P(f_j)\right]\right\rangle + \left\langle log\left[\frac{\chi_2^2}{2}\right]\right\rangle \quad (8)$$

From Abramowitz & Stegun 1964, the estimate of this bias constant is then: $\left\langle log\left[\frac{\chi_2^2}{2}\right]\right\rangle = -0.25068...$, which gives:

$$\left\langle log\left[P(f_j)\right]\right\rangle = \left\langle log\left[I(f_j)\right]\right\rangle + 0.25068 \quad (9)$$

This method is suitable for evenly sampled data, which is not the case for our data. Therefore, we first interpolated the data using a cubic spline interpolation method, and then applied the PSD method on the interpolated light curves. Since the data has been manipulated, we tested our results via simulations.

3.4.2. Simulations

We tested the significance level of the obtained results via simulation. The most used method is the Timmer & König method for light curve simulations (Timmer & Koenig 1995). This method uses a Gaussian distribution to simulate the light curves, which is not the case for the blazar light curves. The burst-like events in blazars deviate considerably from such a distribution and are better described with a gamma or lognormal distribution. This has been taken into account by Emmanoulopoulos et al. 2013, In this paper, we simulated the light curves using the Emmanoulopoulos method using the implementation [11] of (Connolly 2015).

The code calculates the probability density function (PDF) of a given light curve. The estimated PDF is then fitted using a combination of a gamma- and a log-normal distribution. The code also estimates the slope and the normalisation of the PSD,

[11] http://ascl.net/1602.012

using a broken power law model. However these estimates are not reported in this paper since we used a simple power law fit for our PSD fits. Using the best fit parameters, and the slope and normalisation of the PSD, the code simulates a number of light curves that have a PDF similar to the PDF of the original light curve.

3.4.3. PSD parameters test

In order to test our results, a raw fitting on the original PSD is done using the function $P(f) = Nf^{-a}$, (where a is the slope and N the normalisation). After setting the slope and the normalisation as variable in the simulation algorithm (see section. 3.4.2), an interval for each has been defined with an appropriate increment. The next step is to sample the simulated light curves at the same bin width as the observed ones. For each combination of slope and normalisation, a total of two hundred light curve has been simulated. We calculated the PSD of each of these light curves, and calculated the mean and standard deviation of the two hundred PSD as well.

The final step is then to find the combination whose mean fits best the original PSD and minimises the value of the Chi-square (Uttley et al. 2002):

$$\chi^2_{dist} = \sum_{\nu=\nu_{min}}^{\nu_{max}} \frac{[\overline{P_{sim}(\nu)} - P_{obs}(\nu)]^2}{\Delta\overline{P_{sim}(\nu)^2}} \quad (10)$$

By finding the combination that has a minimum Chi-square value, the slope and normalisation of the PSD of a given light curve are then estimated. A simple power-law fit to this PSD was used for the error estimation for simplicity reasons. However, this is not the best approach as the the errors could be significantly underestimated. A more appropriate statistical approach to determine the PSD slopes uncertainties for unevenly sampled data is described in Uttley et al. 2002; Emmanoulopoulos et al. 2013.

3.4.4. PSD results

The variability in AGN light curves resembles various types of noise (Vaughan et al. 2003; Vaughan 2005). The observed variability is a convolution of residual measurement errors and a mixture of the source intrinsic processes, which means that the signal is a result of different statistical noise processes; but in addition, also possible systematic variations (e.g. by physically and geometrically caused variability). The PSD analysis offers the best and the most commonly used method to analyse and investigate the nature of variability. For PSD slopes a close to zero, the variability resembles white noise processes. If the slope is between -1 and -2, the variability is considered to be consistent with red noise processes (Vaughan et al. 2003).

We applied the PSD method on all the observed light curves. Figure 7 shows an example of estimated PSD for the 230 GHz radio light curve; see Figs. A.4 and A.5 for the PSD curves at other frequencies. The black curve is the raw PSD and the green fit curve shows the mean of the PSD values of the two hundred simulated light curves of 230 GHz, with the slope (-1.6) and normalisation (0.005) constant combination that minimised the Chi-square value.

In Fig. 8, we plot the estimated PSD slopes as a function of frequency. A clear decreasing trend can be seen at radio frequencies. The PSD slope at radio bands gets steeper as we go higher in frequency suggesting a higher dominance of red noise at mm-radio bands compared to cm-bands. The PSD slopes get steeper

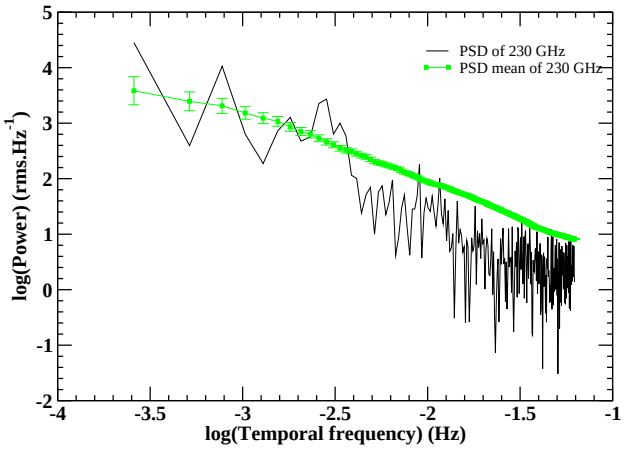

Fig. 7. Best-fitting average power spectrum (in green) superimposed on top of the raw power spectrum at 230 GHz radio band (in black).

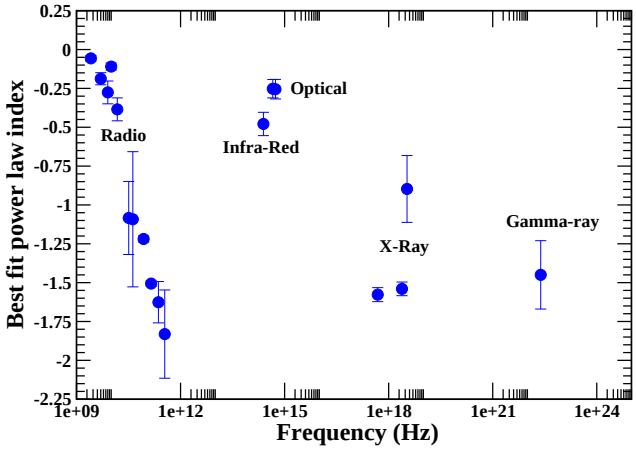

Fig. 8. The best fit power law index plotted as a function of the frequency

as we go to higher frequencies, which is consistent with the fact that at higher radio bands we are probing more and more rapid variations i.e. we are adding more power at higher PSD frequencies. As a consequence, the PSD slope should be flatter rather than steeper. However, this is not the case because of the following: at higher radio frequencies, we observe more flares because the emission region is optically thing. Moreover, there is a contribution of long-term variations in addition to the flares observed in a given time window. We noticed that the PSD slopes at cm-radio bands (a) are consistent with white noise process, which could be well explained by opacity effects i.e. the emission region is opaque at these frequencies. The optical and IR light curves have PSD slopes that are consistent with white noise process.

The X-ray light curves at 2-10 keV band and 10-50 keV band have similar PSD slopes ($a \sim -1.5$), which is also comparable to the slopes at mm-radio bands and at γ-ray energies; intensity variations at these energies are therefore well consistent with red noise process. Variations at hard X-ray bands (14-192 keV) can also be described as red noise process ($a \sim -1$); however, the estimated PSD slope for this band significantly differs from the aforementioned bands. Different PSD slopes could be an indication of different processes responsible for the observed variations.

3.5. Cross-correlation analysis

We used the Discrete Correlation Function method (Edelson & Krolik 1988) to investigate the correlation and possible time lags between two light curves. The first step is to calculate the unbinned discrete correlation function (UDCF) using the given time series for a time lag $\Delta t_{ij} = t_j - t_i$:

$$UDCF_{ij} = \frac{(a_i - \bar{a})(b_j - \bar{b})}{\sqrt{\sigma_a^2 \sigma_b^2}} \quad (11)$$

where a_i and b_j are the individual data points in two different time series, with $\bar{a}$ and $\bar{b}$ being the respective mean value of the time series, and σ_a^2 and σ_b^2 their respective variance. The next step is to bin the UDCF in time. The DCF value for each bin is given as:

$$DCF(\tau) = \frac{1}{M} \sum_{ij} UDCF_{ij}(\tau) \quad (12)$$

where M is the number of data points in each bin. We estimated the error on the DCF using:

$$\sigma_{DCF}(\tau) = \frac{1}{M-1} \sqrt{\sum [UDCF_{ij}(\tau) - DCF(\tau)]^2} \quad (13)$$

This represents the standard deviation of the $UDCF_{ij}$ values within each bin. The DCF value and its error of each interval, is associated to the centre of the bin. The profile of the DCF curves obtained in this paper can be approximated by a Gaussian distribution. As a conservative approach, the FWHM of the fitted Gaussian function is used as an error on the estimated time lag.

To test the significance of the results obtained with the DCF method, we simulated 2000 light curves as it is described in section 3.4.2. The simulated light curves have the same sampling, length, and PSD as the original light curve. We cross-correlated the simulated light curves with the observed light curves in different energy bands. We compared the DCF of the simulated light curves to obtain the 95% confidence level at a given time lag and generated the confidence level curve[12]. In the following section, we will discuss in details the correlation between the broadband light curves.

3.5.1. Radio–radio correlation

As we have noticed in the previous section, the variability is more pronounced at higher radio frequencies. Apparently, the flares at high radio bands lead those at lower energies. To quantify this, we used the DCF method and correlated every observed light curve in the radio bands with the light curve at 230 GHz which is used as a reference frequency because of its high cadence. We also used the 230 GHz light curve to check for correlations with the optical, X-ray, and γ-ray bands. The cross-correlation functions at radio bands are shown in Figs. 9 and A.1. We found a correlation between 230 GHz and all the light curves at frequencies between 23 and 350 GHz. For the light curves at frequencies below 23 GHz, no significant correlation is noticed, which is to be expected as the flaring activity at low frequencies is barely visible. From the DCF analysis, we derive the time lags, which we summarise in Table 2 and Fig. 10. The decreasing time lag with increasing frequency and the negative time lag for the 230 and 350 GHz correlation curve can be expected for the shock-induced flares (Marscher & Gear 1985; Fromm et al. 2011; Rani et al. 2013a).

[12] DCF peaks above the 95% confidence level are considered to be significant

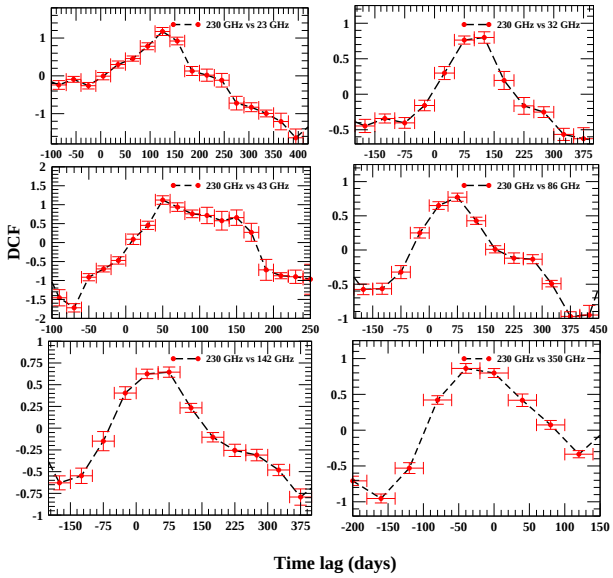

Fig. 9. Plot of the cross-correlation functions of the 230 GHz data vs. the data at 23, 32, 43, 86, 142, and 350 GHz.

Table 2. Measured time lags at radio frequencies as derived from DCF

230 GHz vs.	Time lag (days)
23 GHz	125±15
32 GHz	125±25
43 GHz	50±10
86 GHz	75±25
142 GHz	35±15
230 GHz	0±5
350 GHz	-(40±20)

The positive time lag indicates that the flaring activity at 230 GHz band is leading and vice-versa.

Figure 10 shows the estimated time lag between the 230 GHz and the other radio light curves, plotted as a function of frequency. The decreasing trend can be described by a power-law of the form $f(\nu) = N\nu^{-\frac{1}{k_r}}$ (Kudryavtseva et al. 2011). The power-law fitting gives k_r=(1.12±0.46), and the grey shaded area represents the error interval on the fit. A value $k_r \sim 1$ suggests equipartition between the magnetic field and the electron energy density in the emission region (Lobanov 1998). The lack of correlation between 230 GHz and the lower radio frequencies (below 23 GHz) could be due to synchrotron-self absorption, where opacity effects dominate.

The estimated time lag could be translated into separation of the two emission regions using (Fuhrmann et al. 2014):

$$\Delta r_{\gamma,r} = \frac{\beta_{app} c \tau_{\gamma,r}}{sin\theta} \quad (14)$$

where β_{app} is the apparent speed, c is the speed of light, θ is the viewing angle, and $\tau_{\gamma,r}$ is the obtained time lag. The apparent speed β_{app} has values ranging from 5 to 15 for its different component (Savolainen et al. 2006; Lister et al. 2013). In this paper, we adopt an averaged β_{app} value of 7, and for the viewing angle θ=9.8° (Savolainen et al. 2006).

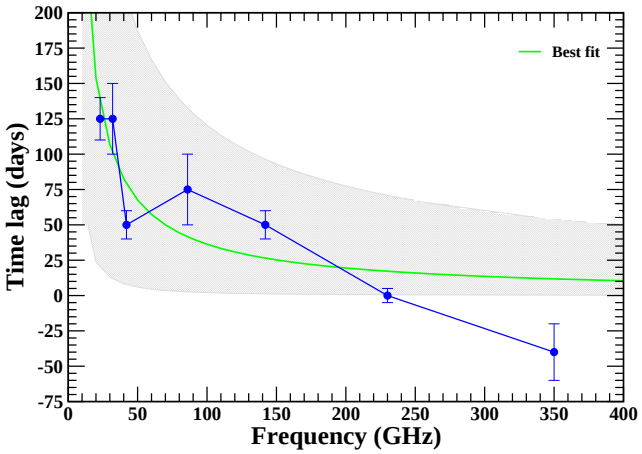

Fig. 10. Time lag relative to the curve at 230 GHz plotted as a function of radio frequencies (in blue). The green curve represent the best power law fit of the data points, with a slope of k_r=1.12±0.46. The grey shaded area represents the error interval on the fit.

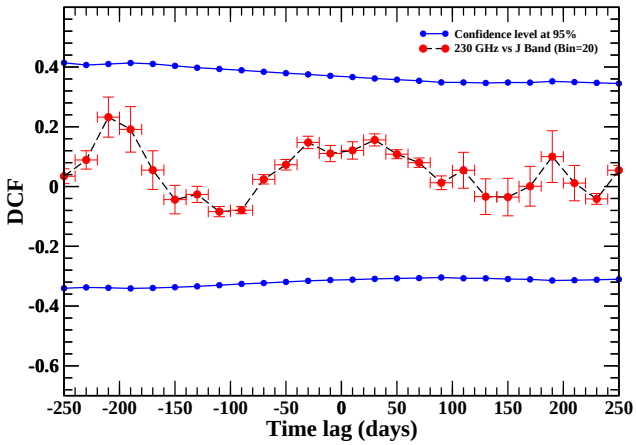

Fig. 11. DCF analysis curve for 230 GHz vs. J passband. The blue curve represents the 95% confidence level.

A recent jet kinematics study suggests that the location of the 7 mm (43 GHz) VLBI core is at a distance of 4–7 pc from the jet apex using core-shift measurements (Lisakov et al. 2016, in prep). The correlation between 230 GHz and 43 GHz showed a time lag of (50±10) days. This translates, by applying eq. 14, to a relative separation of (1.7±0.3) pc. Therefore, we estimate that the 230 GHz emission region is at (5.3±0.3) pc from the jet apex.

3.5.2. Radio-optical correlation

Unlike the radio light curves, the light curves at optical and IR passbands do not show any significant variability. Therefore, we cannot detect any significant correlation between radio and optical/IR light curves. In Fig. 11, we show the cross-correlation analysis curve between radio (230 GHz) and J passband.

3.5.3. Radio – X-ray correlation

Similar fractional variability amplitudes and PSD slopes for mm-radio band and X-ray light curves suggest a possible correlation between the two. To quantify this, we applied the DCF analysis method and correlated the X-ray light curves at 14-192 keV and at 2-10 keV with the radio light curve at 230 GHz. The DCF curves are shown in Fig. 12. The peaks of the DCF curves are above the 95% confidence level. This implies that the X-ray light curves at different bands correlate significantly with the radio light curve at 230 GHz. We notice a peak at a time lag of (90±10) days for the correlation curve between X-ray 14-192 keV and 230 GHz, with a coefficient of (0.7±0.2) with the X-ray emission leading the radio emission. This time lag translates to 3.1±0.4 pc relative distance, by applying eq. 14. For the DCF curve between X-ray 2-10 keV and 230 GHz, we measured a peak at a time lag of (10±10) days with the X-ray emission leading the radio emission and a correlation coefficient of (0.5±0.3) giving a relative distance of (0.4±0.4) pc. Similar results have been found for the correlation between 10-50 keV and 230 GHz, implying that the two emission regions at X-ray energies 2–10 and 10–50 keV are co-spacial.

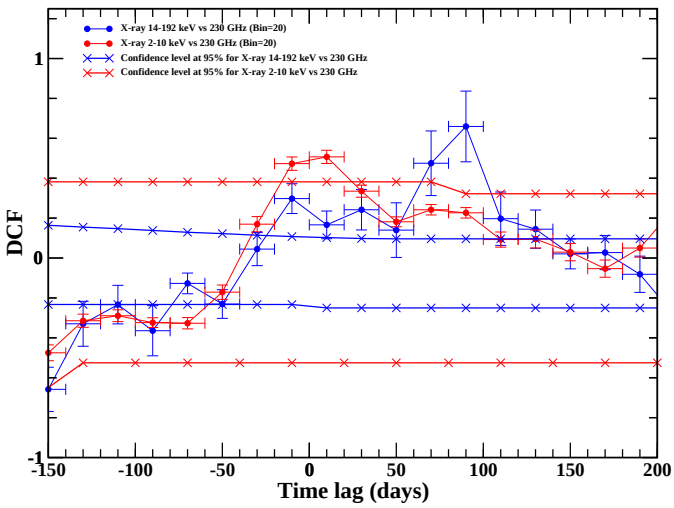

Fig. 12. DCF curves of: X-ray at 14-192 keV vs. 230 GHz (blue) and X-ray at 2-10 keV vs. 230 GHz (red).

3.5.4. Radio – gamma-ray correlations

As mentioned in section 3, there is an apparent correlation between the mm-radio and γ-ray light curves. To quantify this, we correlated the weekly sampled γ-ray light curve with the radio light curve at 230 GHz. Figure 13 shows the DCF curve between γ-rays and 230 GHz light curve for the entire data set. The DCF curve shows a broad and prominent peak at a time lag of 110± 27 days, suggesting that the γ-rays lead the radio emission by ~110 days. However, the formally calculated significance of the cross-correlation falls below 95%, with regard to the whole data set. Since both radio and γ-ray light curves consist of many flares, the DCF analysis of the entire data set shows an average behaviour of different variability features. This could be due to the blending effect of the two flares $\mathcal{R}_1$ and $\mathcal{R}_2$ in the radio bands. However, when we restrict the DCF analysis to the time ranges of the individual flares $\mathcal{R}_1$ and $\mathcal{R}_2$, we found a significant correlation between the two.

For the first flare, the DCF curve shows a peak at 120±25 days, confirming that the γ-rays lead the radio emission. For the second flare, the DCF curve has a peak at (95±16) days. This suggests that the γ-ray emission is leading the radio emission, placing, the γ-ray emission region closer to the jet apex than the radio emission regions. Using eq. 14, a time lag of be-

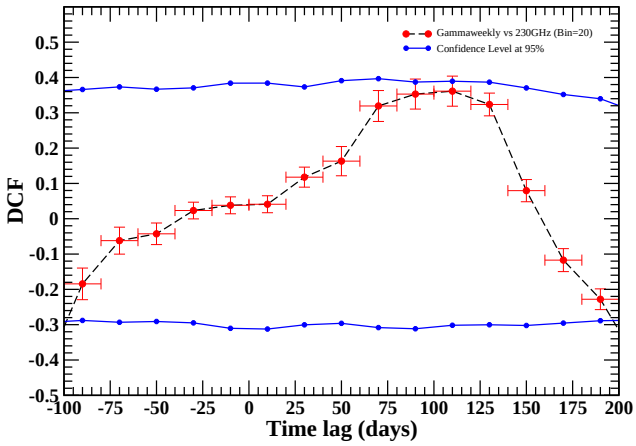

Fig. 13. DCF curve of γ-ray and 230 GHz light curves - for the full data. The blue lines represent the 95% significance levels.

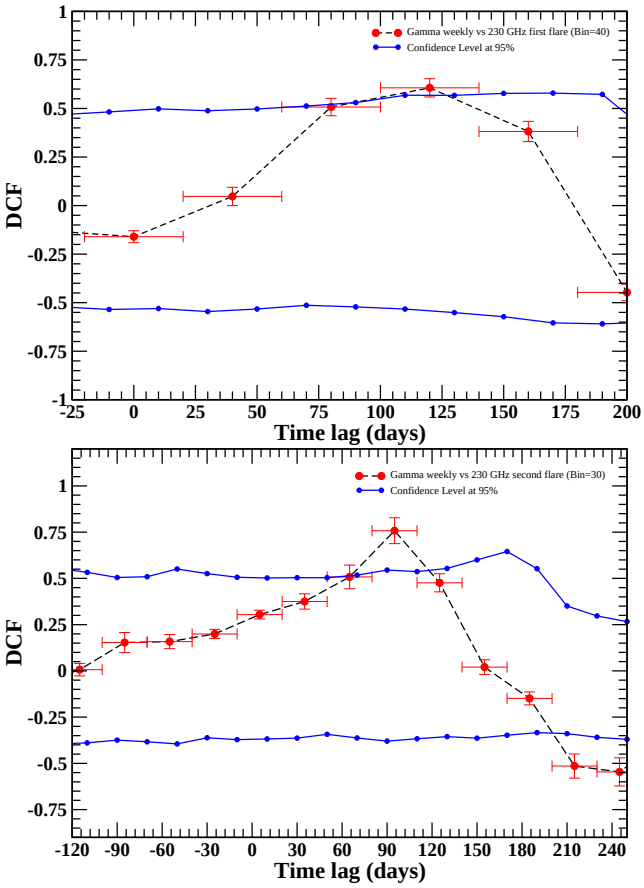

Fig. 14. DCF curve of γ-ray and 230 GHz during the first flare (top); DCF curve of γ-ray and 230 GHz during the second flare (bottom). The blue lines represent the 95% confidence levels.

tween 90 and 120 days gives an offset of $\Delta r_{\gamma,r}$ between 3.1 and 4.1 pc.

3.5.5. Optical - X-ray correlation

The X-ray light curves show strong variability across the observation period, which is not the case for the optical/IR light curves. The absence of a prominent peak in the optical/IR light curves, does not allow us to make any claims about a correlation between the optical/IR and X-ray bands. A formal cross-correlation analysis between the two bands does not show any peak.

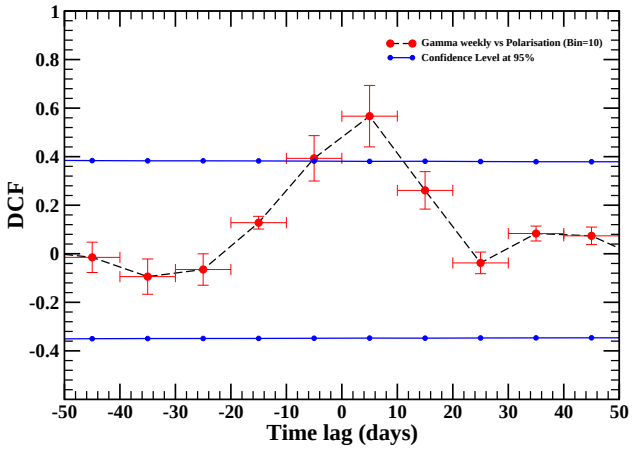

Fig. 15. DCF curve of γ-ray light curve and optical percentage polarisation. The blue lines represent the 95% confidence levels.

3.5.6. Optical/IR - Gamma-ray correlation

As shown in Fig. 1, the optical/IR light curves are not variable during the period of flaring activity in the GeV regime. The DCF analysis shows that there is no correlation between the two bands. Similar results are obtained for the correlation between γ-ray and the optical R band, and between γ-ray and the infra-red J band. This suggests different physical mechanisms and causally disconnected emission regions for γ-rays and optical frequencies. However, it is important to note the data gap in the optical/IR light curve during the γ-ray flares, since from an observational point of view, a simultaneous variability or delay cannot be discarded.

Although the polarisation observations in optical band are not as well sampled as the γ-ray light curve, there is a hint of an apparent correlation between the two. For instance, we noticed prominent variations in the polarisation curve during the γ-ray flaring activity period. In addition to that, no variation is apparent in the polarisation curve during the quiescent phase in the GeV regime (see Fig. 1). To quantify the apparent correlation, we applied the DCF analysis method. The DCF curve is shown in Fig. 15. The DCF curve shows a peak at a time lag of 5±5 days, which suggests a significant correlation between the two. It is important to note that there is a data gap in the percentage polarisation data between MJD = 55000 and 55150 and between MJD = 55400 and 55500. Therefore, it is essential to test this correlation using simultaneous observations.

3.5.7. X-ray - X-ray correlations

The X-ray light curves in the three different bands showed strong and similar variability behaviour across the observation time. We cross-correlated the X-ray light curve at 14-192 keV with the X-ray light curves at 2-10 keV band and 10-50 keV band. The DCF results in Fig. 16, show a correlation between the three X-ray bands. A peak close to 0 time lag is observed in the three DCF curves

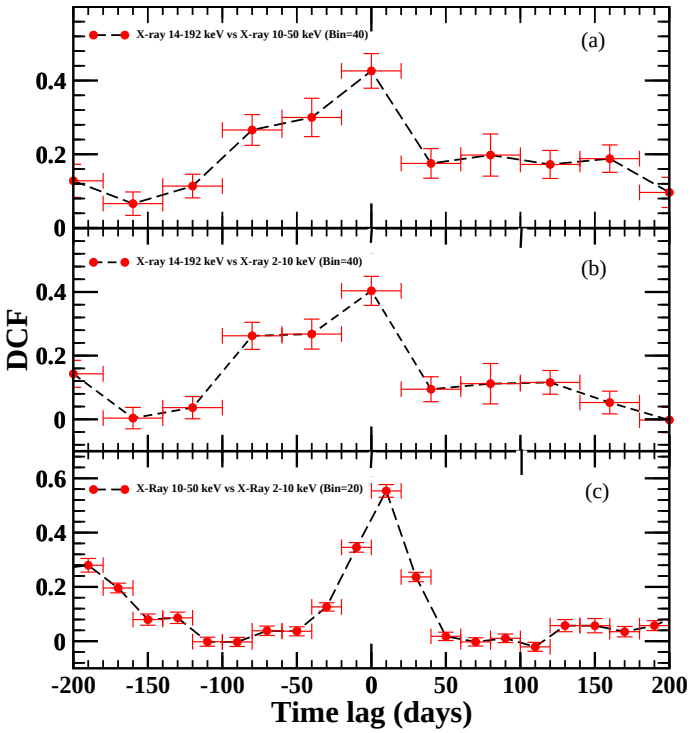

Fig. 16. DCF curves of the different X-ray bands: 14-192 keV vs. 10-50 keV (a), 14-192 keV vs. 2-10 keV (b), and 10-50 keV vs. 2-10 keV (c).

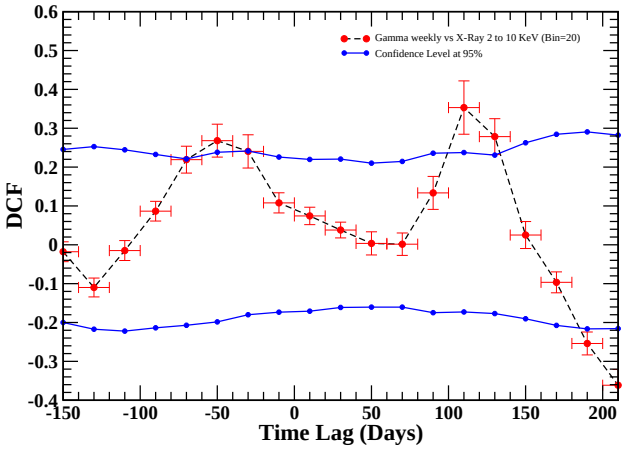

Fig. 17. DCF curve of γ-ray and X-Ray 2-10 keV band. The blue lines represent the 95% confidence levels.

3.5.8. X-ray - γ-ray correlation

The source exhibits prominent flaring activity at both X-ray and γ-ray energies. The DCF curve between γ-ray and the X-ray light curve at 2-10 keV band is show in Fig. 17. The DCF curve shows two peaks, at a time lag -(50±10) days and (110±10) days. The positive time lag (~ 100 days) suggests that the γ-ray is leading the X-ray emission. The negative time lag (~ -50 days) suggests that the X-ray emission is leading the γ-ray emission. The estimated time lags suggests the following two possible scenarios:

1. Scenario 1: X-rays are leading the γ-ray emission with a time lag of −(50±10) days, which translate to a de-projected distance of (1.7±0.3) pc using eq. 14. The X-ray emission region is therefore closer to the jet apex than the γ-rays emission region.
2. Scenario 2: gamma-rays are leading the X-ray emission with a time lag of 110±10 days, corresponding to a distance of (3.8±0.3) pc. The γ-ray emission region is then closer to the jet apex than the X-rays emission region, or, in other words, the γ-rays are further up stream, and the X-ray are emitted from a region downstream the jet.

4. Discussion

Using the broadband variability study of the FSRQ 3C 273 observed between May 2008 and March 2012, we investigated the connection between flaring activity at GeV and lower energies. We also put constraint on the location and size of emission regions at different frequencies. The ultimate goal of the study is to provide a general physical scenario by which the observed variations of the source across several decades of frequencies can be put in a consistent context.

4.1. Radio emission

The radio data collected between 2.6 to 350 GHz allow us to perform a detailed study of flaring activity at radio bands. Two major outbursts ($\mathcal{R}_1$ and $\mathcal{R}_2$) were detected in the source during the course of our observations. We found a significant correlation between the multi-band radio data such that the flaring activity at higher radio frequencies lead those at lower frequencies. These results can be explained in the frame of the shock-in-jet-model (Marscher & Gear 1985). There was no pronounced flaring activity at radio bands below 23 GHz. The fractional variability showed an increasing trend with increasing radio frequencies. The PSD slopes suggests that the lower radio frequency variations are dominated by white noise processes. We then used the cross-correlation results between 43 and 230 GHz to locate the emission region at 230 GHz, which we found is about (5.3±0.3) pc from the jet apex.

4.2. Optical/IR emission

Compared to the other frequencies, the observed flaring activity is significantly lower at optical and IR regime. The estimated fractional variability amplitude is lower than 13%. In addition to that, the optical/IR light curves do not exhibit a significant correlation with the observed light curves at other frequencies (which could also be due to the gap in the optical data). The power spectral density (PSD) slope results show a power law index close to zero, which is consistent with the slope of a white noise process. Spectral studies done on the optical/IR emission showed that this emission, particularly the excess emission at UV bands causing the blue bump, is dominated by thermal emission from the accretion disk (Shields 1978; Soldi et al. 2008). Alternatively the presence of a X-ray source or a hot corona could contribute significantly to the optical/UV emission (Collin-Souffrin 1991; Haardt et al. 1994).

4.3. Gamma-ray emission

The source 3C 273 showed a prominent flaring activity at GeV energies during a period between July 2009 and April 2010. Our analysis suggests a significant correlation between the γ-rays and the 230 GHz light curve, with a time lag of (110±27) days, which translates to a relative separation between γ-ray and 230 GHz

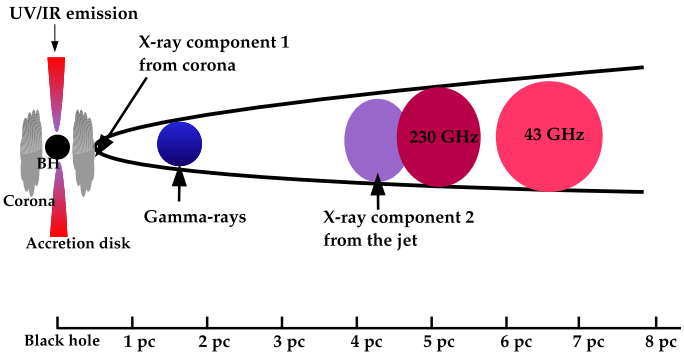

Fig. 18. Sketch representing the location of the emission regions at different frequencies.

emission region of around (3.8±0.9) pc. The radio correlation between 43 and 230 GHz puts the location the 230 GHz emission region at a distance of (5.3±0.3) pc from the jet apex. This places the γ-ray emission region at a distance of (1.2±0.9) pc from the jet apex. This result is in agreement with the result found in Rani et al. 2013b that constrained the γ-ray emission region to < 1.6 pc from the jet apex.

The fractional variability amplitude in the radio bands is around 40%, whereas, the γ-ray light curves showed a fractional variability amplitude of around 100%. The PSD slope at mm-radio bands and γ-ray energies are however similar, and are consistent with the slopes of a red noise process. Moreover, the longest time scale of variability at high radio frequencies is very similar to that at γ-ray energies, implying thus, a similar size of the emission region for the two energy ranges. The fastest variability time scale for γ-rays frequency is 1.1 hour (Rani et al. 2013b), suggesting then, the presence of several very compact emission regions at γ-ray energy bands, as it is expected in the multi-zone emission model suggested by Marscher 2014.

The spectral changes reported in Rani et al. 2013b suggests an external Compton mechanism with seed photons from the broad line region (BLR). The optical polarisation has significantly increased during the γ-ray flaring activity, suggesting thus a possible correlation between the γ-rays and the optical polarisation. This indicates that the non-thermal emission component and the γ-ray emission are linked. A detailed broadband spectral energy distribution (SED) modeling will shed more light on SSC (synchrotron self-Compton) and EC (external-Compton) contribution.

4.4. X-ray emission

In comparison to a brief episode of flaring activity (July 2009 to April 2010) followed by a quiescence phase at radio and γ-ray frequencies, the X-ray regime was dominated by episodes of repeated variability. The DCF curve between γ-rays and X-rays shows two time lags, one being negative of −(50±10) days, and another being positive with a time lag of 110±10 days. The DCF analysis suggests the presence of two possible components that are responsible for the X-ray emission. The negative time lag suggests the X-ray emission is leading the γ-ray emission, and is located at a distance of 0.1 to 0.5 pc from the jet apex. The positive time lag suggests that the γ-ray emission is leading the X-ray emission with a corresponding separation distance of around (3.8±0.3) pc. This component could be emitted from the jet through inverse-Compton processes. An independent study of the X-ray spectrum also suggests the presence of two components. A component coming from a hot corona or reflected off an accretion disk, accounting for the presence of the weak iron line found in the X-ray spectrum at 3-78 keV, and a second component most likely coming from the jet that starts to dominate at 30-40 keV (Madsen et al. 2015).

The two component scenario for the X-ray emission is also confirmed by X-ray vs. radio correlation analysis. We noticed similar fractional variability amplitudes for the three X-ray bands and the mm-radio bands. The PSD slopes are also comparable for the mm-radio bands and X-ray at 2-10 keV and 10-50 keV. The SF analysis showed the presence of a quasi-periodic variability for both X-ray and mm-radio light curves. Correlation analysis suggests a time lag of 90±10 days between 14-192 keV X-ray light curve and 230 GHz light curve, which translates to 3.1±0.4 pc placing the location of the X-ray emission region at 0.5 to 2 pc from the jet apex. The DCF curve between X-rays at 2-10 keV and 230 GHz shows a time lag of (10±10) days, which gives a relative distance between the X-ray and radio emission regions of (0.4±0.4) pc. This provides an estimate of the location of 2-10 keV X-ray emission at 4.7±0.4 pc from the jet apex. We obtained similar results for the intensity variations at 10-50 keV X-ray band.

The longest time scale of variability for the X-ray light curves is ∼230 days. To estimate the size of the emission region, we applied (Rani et al. 2013b):

$$R \leq \frac{c \times t_{var} \times \delta}{1+z} \tag{15}$$

where R is the size of the emission region, t_{var} is the shortest time scale of variability, c is the speed of light, δ is the Doppler factor of the source for which we used a value of 7 (Savolainen et al. 2006), and z is the red-shift of the source. For a time lag of ∼230 days, we obtained an emission region with a size of ∼1.2 pc. The size of this emission region is much bigger than the size of the corona, which was suggested to be around 20-30 R_S (0.013-0.02 pc) (Reis & Miller 2013) where $R_S = 6.4 \times 10^{-4}$ pc is the Schwarzschild radius of the black hole where the mass of supermassive black hole of 3C 273 is around 6.6×10^9 $M_\odot$ (Paltani & Türler 2005). However, we noticed that for the X-ray light curves used in this study, the shortest variability time scale is ∼ 5-10 days. This gives translates to a size of 0.025 – 0.05 pc, which is comparable to the size of the corona. This implies, that the long term variability is probably coming from the jet, whereas the faster variability seems to be originated closer to the black hole.

4.5. Broadband correlation alignment

The statistical analysis presented in this paper suggests a causal connection between the observed broadband flaring activity in the source. The proposed scenario is presented in Fig. 18 where we marked the location of different emission regions. A moving shock/disturbance propagating downstream of the jet could first produce the γ-ray flares at a distance of ∼1.2 pc, and later could brighten the emission region at mm-radio bands. The mm-radio flares lead those at cm-radio bands. Delayed emission at cm-radio bands is a clear indication of opacity effects due to synchrotron self-absorption. Our analysis suggests two possible components responsible for the X-ray emission. One component of the X-ray emission is most likely coming from the hot corona or jet-apex. The second X-ray component seems to have non-thermal origin i.e. produced via inverse-Compton scattering of

radio synchrotron photons at a distance of ∼4.7 pc from the jet-apex. Observations at optical/IR regime suggests a prominent thermal dominance either from the accretion disk or/and from the BLR region.

5. Conclusion

In this paper, we presented the results of our broadband variability study of the FSRQ 3C 273 observed for a time period between May 2008 and March 2012. A detailed statistical analysis was performed to constrain the location of the emission region at different energy bands and to explore the connection between the broadband flaring activity.

The source went through a series of rapid flares at the γ-rays which has been been accompanied by flaring activity at other energies. We studied the broadband variability behaviour of 3C 273, by comparing the general behaviour and the properties of the light curves at different energy bands. Except for the light curves at cm-radio and optical/IR frequencies, the observed broadband variations are found to be consistent with red-noise processes. Absence of a pronounced flaring activity at at cm-radio bands could be due to synchrotron self-absorption, and at optical/IR bands, it could be because of the dominance of thermal emission. The optical/IR emission seems to be dominated by thermal emission from the disk and/or the BLR.

At radio bands, the fractional variability amplitude increases with increase in frequency, while the variability time scale decreases implying that at higher frequencies, we are probing more compact emission regions. In addition to that the variability time scales are found to be very similar at different regimes. The estimated fractional variability seems to follow a double hump structure as a function of frequency, which suggests that the largest variations are seen for the highest energy photons.

The evolution of radio flares could be well explained in the frame of the shock-in-jet model. From the correlation analysis, we found that the 230 GHz radio flares are emitted at a distance between 5.3 pc from the jet apex. The γ-ray energies are emitted from a compact region at a distance ∼ 1.2 pc from the jet apex, through IC processes. There seem to be two components responsible for the X-ray emission. The first component is located within a distance of 0.1–0.5 pc from the jet apex and most likely emitted either by the corona or regions closer to the jet apex. The second component responsible for X-ray emission is located at a distance of ∼4.7 pc and is produced through up-scattering of radio synchrotron photons via IC processes. A broadband spectral energy density analysis can provide better constrains on the different emission mechanisms that are taking place in the jet.

Acknowledgements. CC was supported for this research through a stipend from the International Max Planck Research School (IMPRS) for Astronomy and Astrophysics at the Universities of Bonn and Cologne. The authors would like to thank Dimitris Emmanoulopoulos, Sam Connolly, and Walter Max-Moerbeck for useful discussions on statistical analysis and for their suggestions and comments on the paper draft. This research is partly based on observations with the 100-m telescope of the MPIfR (Max-Planck-Institut für Radioastronomie) at Effelsberg. The *Fermi*-LAT Collaboration acknowledges generous ongoing support from a number of agencies and institutes that have supported both the development and the operation of the LAT as well as scientific data analysis. These include the National Aeronautics and Space Administration and the Department of Energy in the United States, the Commissariat à l'Energie Atomique and the Centre National de la Recherche Scientifique / Institut National de Physique Nucléaire et de Physique des Particules in France, the Agenzia Spaziale Italiana and the Istituto Nazionale di Fisica Nucleare in Italy, the Ministry of Education, Culture, Sports, Science and Technology (MEXT), High Energy Accelerator Research Organization (KEK), and Japan Aerospace Exploration Agency (JAXA) in Japan, and the K.∼A.∼Wallenberg Foundation, the Swedish Research Council, and the Swedish National Space Board in Sweden. Additional support for science analysis during the operations phase is gratefully acknowledged from the Istituto Nazionale di Astrofisica in Italy and the Centre National d'Études Spatiales in France. The optical/IR observations are provided by the Yale *Fermi*/SMARTS project. Data from the Steward Observatory spectropolarimetric monitoring project were used. This program is supported by *Fermi* Guest Investigator grants NNX08AW56G, NNX09AU10G, NNX12AO93G, and NNX15AU81G. The Submillimeter Array is a joint project between the Smithsonian Astrophysical Observatory and the Academia Sinica Institute of Astronomy and Astrophysics and is funded by the Smithsonian Institution and the Academia Sinica. This research is partly based on observations carried out with the IRAM 30m telescope. IRAM is supported by INSU/CNRS (France), MPG (Germany) and IGN (Spain).

References

Abdo, A. A., Ackermann, M., Agudo, I., et al. 2010, ApJ, 716, 30
Abramowitz, M. & Stegun, I. 1964, Handbook of Mathematical Functions, Applied Mathematics Series, Vol. 55, New York, Dover Publications
Angelakis, E., Fuhrmann, L., Marchili, N., Krichbaum, T. P., & Zensus, J. A. 2008, MEMSAI, 79, 1042
Beaklini, P. P. B. & Abraham, Z. 2014, MNRAS, 437, 489
Bonning, E., Urry, C. M., Bailyn, C., et al. 2012, ApJ, 756, 13
Chernyakova, M., Neronov, A., Courvoisier, T. J.-L., et al. 2007, A&A, 465, 147
Collin-Souffrin, S. 1991, A&A, 249, 344
Connolly, S. D. 2015 [arXiv:1503.06676]
Edelson, R. A. & Krolik, J. H. 1988, ApJ, 333, 646
Emmanoulopoulos, D., McHardy, I. M., & Papadakis, I. E. 2013, MNRAS, 433, 907
Emmanoulopoulos, D., McHardy, I. M., & Uttley, P. 2010, MNRAS, 404, 931
Fromm, C. M., Perucho, M., Ros, E., et al. 2011, A&A, 531, A95
Fuhrmann, L., Larsson, S., Chiang, J., et al. 2014, MNRAS, 441, 1899
Fuhrmann, L., Zensus, J. A., Krichbaum, T. P., Angelakis, E., & Readhead, A. C. S. 2007, in AIPC, Vol. 921, The First GLAST Symposium, ed. S. Ritz, P. Michelson, & C. A. Meegan, 249–251
Geweke, J. & Porter-Hudak, S. 1989, Journal of Time Series Analysis
Grandi, P. & Palumbo, G. G. C. 2004, Science, 306, 998
Gurwell, M. A., Peck, A. B., Hostler, S. R., Darrah, M. R., & Katz, C. A. 2007, in ASPC, Vol. 375, From Z-Machines to ALMA: (Sub)Millimeter Spectroscopy of Galaxies, ed. A. J. Baker, J. Glenn, A. I. Harris, J. G. Mangum, & M. S. Yun, 234
Haardt, F., Maraschi, L., & Ghisellini, G. 1994, ApJL, 432, L95
Hartman, R. C., Bertsch, D. L., Fichtel, C. E., et al. 1992, in NASA Conference Publication, Vol. 3137, NASA Conference Publication, ed. C. R. Shrader, N. Gehrels, & B. Dennis
Ikejiri, Y., Uemura, M., Sasada, M., et al. 2011, PASJ, 63, 639
Jahoda, K. 1994, in Bulletin of the American Astronomical Society, Vol. 26, AAS #184, 894
Jorstad, S., Marscher, A., Smith, P., et al. 2012, International Journal of Modern Physics Conference Series, 8, 356
Kudryavtseva, N. A., Gabuzda, D. C., Aller, M. F., & Aller, H. D. 2011, MNRAS, 415, 1631
Lister, M. L., Aller, M. F., Aller, H. D., et al. 2013, AJ, 146, 120
Liu, W.-P. & Shen, Z.-Q. 2009, RAA, 9, 520
Lobanov, A. P. 1998, A&A, 330, 79
Madsen, K. K., Fürst, F., Walton, D. J., et al. 2015, ApJ, 812, 14
Marscher, A. P. 2014, ApJ, 780, 87
Marscher, A. P. & Gear, W. K. 1985, ApJ, 298, 114
Max-Moerbeck, W., Hovatta, T., Richards, J. L., et al. 2014, MNRAS, 445, 428
McHardy, I., Lawson, A., Newsam, A., et al. 1999, MNRAS, 310, 571
McHardy, I., Lawson, A., Newsam, A., et al. 2007, MNRAS, 375, 1521
Paltani, S., Courvoisier, T. J.-L., & Walter, R. 1998, A&A, 340, 47
Paltani, S. & Türler, M. 2005, A&A, 435, 811
Papadakis, I. E. & Lawrence, A. 1993, MNRAS, 261, 612
Ramakrishnan, V., Hovatta, T., Nieppola, E., et al. 2015, MNRAS, 452, 1280
Rani, B., Krichbaum, T. P., Fuhrmann, L., et al. 2013a, A&A, 552, A11
Rani, B., Lott, B., Krichbaum, T. P., Fuhrmann, L., & Zensus, J. A. 2013b, A&A, 557, A71
Rani, B., Wiita, P. J., & Gupta, A. C. 2009, ApJ, 696, 2170
Reis, R. C. & Miller, J. M. 2013, ApJ, 769, L7
Robson, E. I., Litchfield, S. J., Gear, W. K., et al. 1993, MNRAS, 262, 249
Ross, R. R. & Fabian, A. C. 1993, MNRAS, 261, 74
Savolainen, T., Wiik, K., Valtaoja, E., & Tornikoski, M. 2006, A&A, 446, 71
Schmidt, M. 1963, Nature, 197, 1040
Shields, G. A. 1978, Nature, 272, 706
Simonetti, J. H., Cordes, J. M., & Heeschen, D. S. 1985, ApJ, 296, 46
Smith, P. S., Montiel, E., Rightley, S., et al. 2009, ArXiv e-prints [arXiv:0912.3621]
Sokolov, A. & Marscher, A. P. 2005, ApJ, 629, 52
Soldi, S., Türler, M., Paltani, S., et al. 2008, A&A, 486, 411

Stroh, M. C. & Falcone, A. D. 2013, ApJS, 207, 28
Timmer, J. & Koenig, M. 1995, A&A, 300, 707
Türler, M., Courvoisier, T. J.-L., & Paltani, S. 1999, A&A, 349, 45
Uchiyama, Y., Urry, C. M., Cheung, C. C., et al. 2006, ApJ, 648, 910
Uemura, M. & Kanata Team. 2009, in ASPC, Vol. 404, The Eighth Pacific Rim Conference on Stellar Astrophysics: A Tribute to Kam-Ching Leung, ed. B. Soonthornthum, S. Komonjinda, K. S. Cheng, & K. C. Leung, 69
Uttley, P., McHardy, I. M., & Papadakis, I. E. 2002, MNRAS, 332, 231
Valtaoja, L., Takalo, L. O., Sillanpaa, A., et al. 1991, AJ, 102, 1946
Vaughan, S. 2005, A&A, 431, 391
Vaughan, S., Edelson, R., Warwick, R. S., & Uttley, P. 2003, MNRAS, 345, 1271
Walter, R. & Courvoisier, T. J.-L. 1992, A&A, 258, 255

Appendix A: Structure function, cross-correlation analysis, and PSD plots

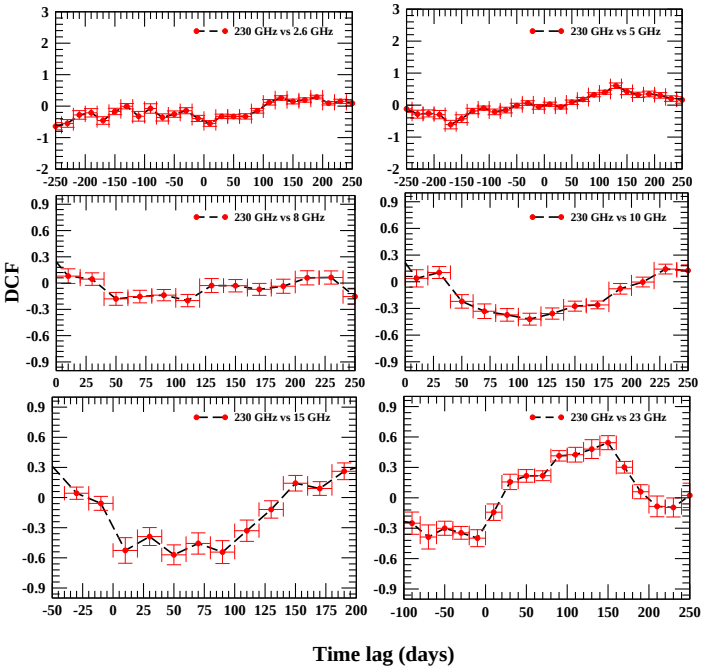

Fig. A.1. Cross-correlation analysis curves at radio frequencies (230 GHz vs. 2.6, 5, 8, 10, 15, and 23 GHz).

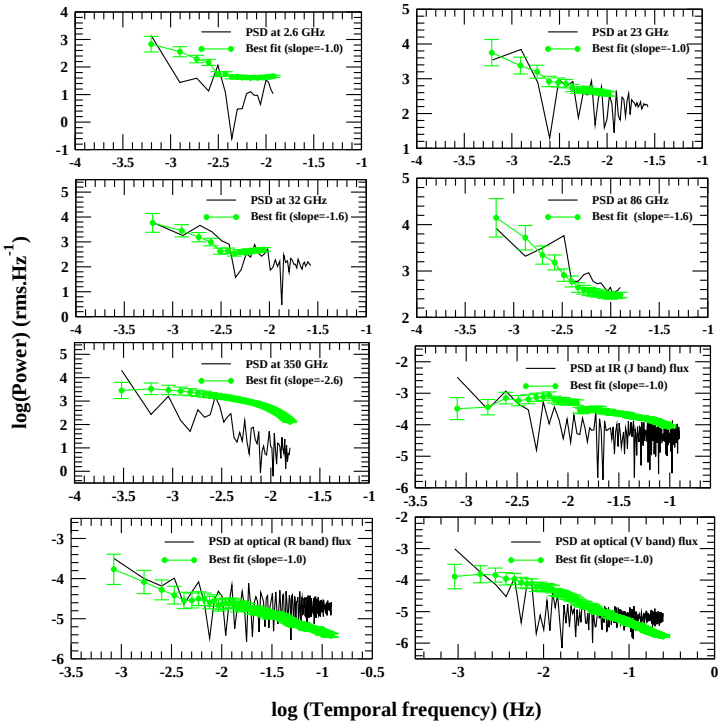

Fig. A.4. PSD curves at radio (2.6 to 350 GHz), IR (J band), optical (R and V bands), X-ray, and γ-ray frequencies.

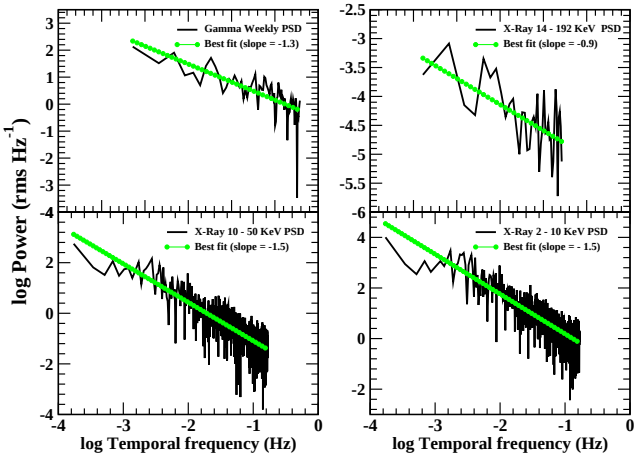

Fig. A.5. PSD curves at X-ray and γ-ray frequencies.

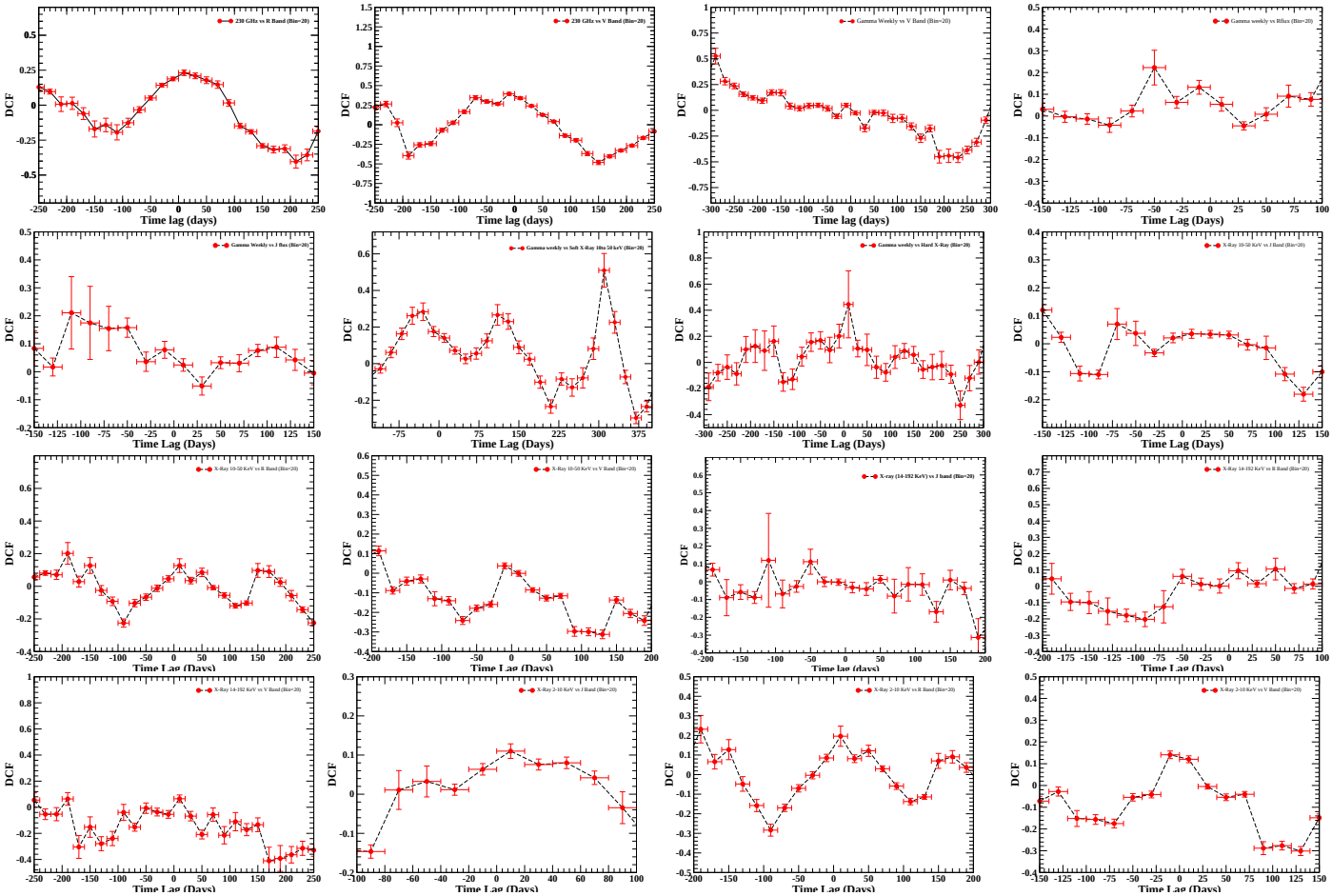

Fig. A.2. Cross-correlation analysis curves.

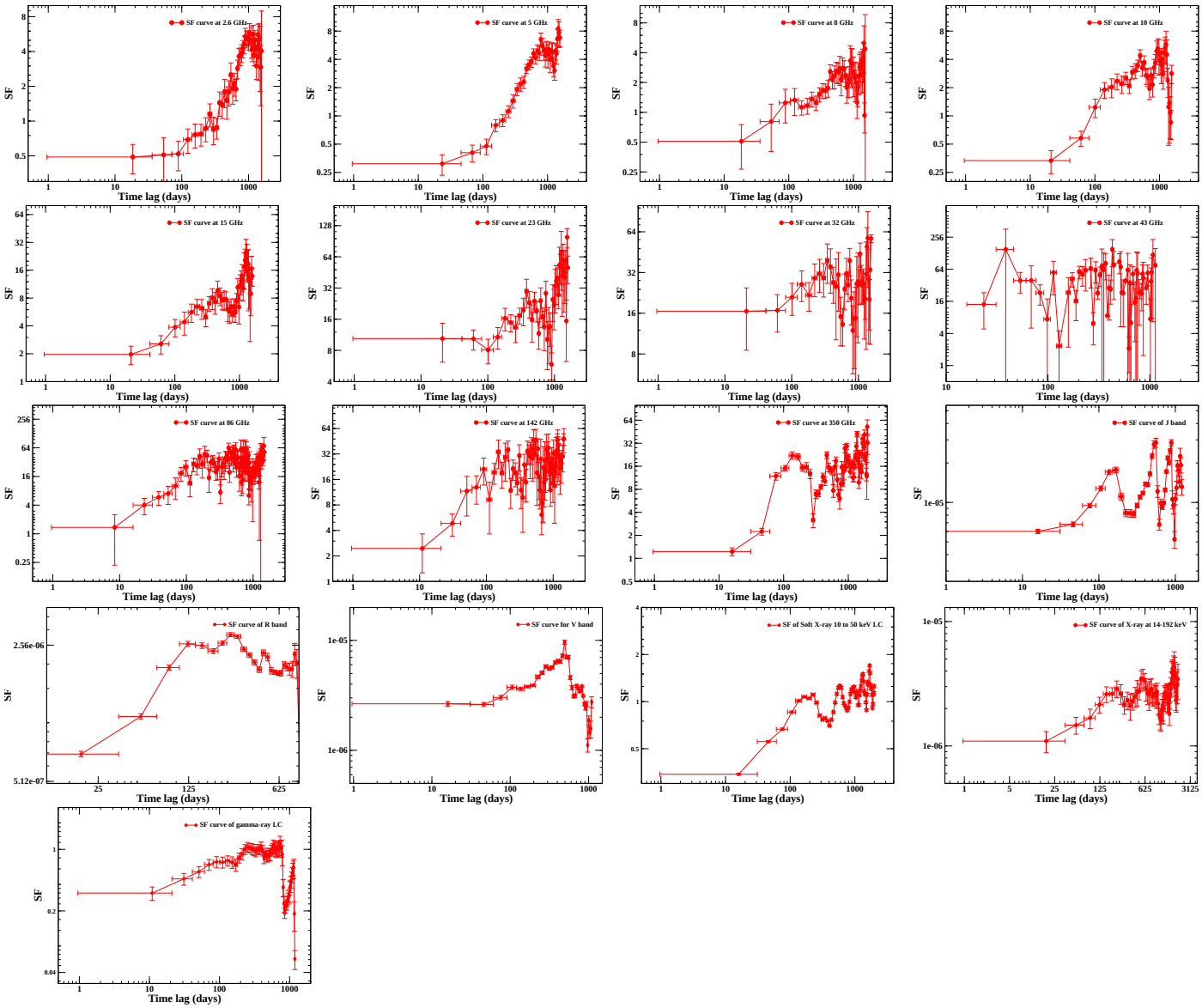

Fig. A.3. Structure function curves at radio (2.6 to 350 GHz bands), IR (J band), optical (R and V bands), X-ray (10 – 50 keV and 14 – 192 keV), and γ-ray frequencies.